Optical cavities and quantum emitters

Koks, C.

6

PROBING MICROCAVITY RESONANCE SPECTRA WITH INTRACAVITY EMITTERS

We measure the fluorescence spectrum of broadband emitters in an optical microcavity with radius of curvature $R = 17.7(3)$ μm and finesse $F \approx 1000$. By measuring these cavity emission spectra as a function of cavity length, we obtain a rich and complete picture of the optical microcavity. First, we can accurately determine the penetration depths of the cavity mirrors. Second, we measure a mode splitting within each transverse mode group, which can dominantly be assigned to mirror astigmatism. Third, we observe and quantify mode coupling between fundamental and higher-order transverse modes. The chapter thus shows how the analysis of emission spectra as a function of cavity length can be used to fully characterize the optical microcavity.

C. Koks and M. P. van Exter (submitted for publication)

6.1. INTRODUCTION

Optical microcavities [23] are widely used in optics, for instance, to create good single photon sources [10, 29, 50, 77], to image surface layers with very high precision [30–32], to simulate physical processes like Bose-Einstein condensates [113] or non-equilibrium dynamics [114], and to perform chemical sensing [44, 76]. All these examples require many reflections between the mirrors of the cavity, while maintaining strong (transverse) field confinement. In the past decade, open microcavities have been developed for this purpose [65]. In open microcavities, the two mirrors can be tuned individually to vary the cavity length and lateral mirror displacement.

Accurate measurements of the optical modes in a microcavity reveal valuable information about mirror reflections. Especially microcavities with a small mode waist and a large finesse F show interesting physical behavior. The resonant mode spectra are grouped in a fundamental mode and higher-order transverse mode groups. The structure of these mode groups reveals information about the microcavity. Even microcavities with ideal mirrors have a mode spectrum, which is created by nonparaxial and polarization effects [60, 88, 110]. These effects are intrinsic and occur in all cavities. The associated mode spectrum is called a fine structure. This mode spectrum changes when imperfect mirrors are used, for instance, cavities with astigmatic mirrors show a mode-spectrum with almost equidistant mode spacings. Most often, a combination of the nonparaxial fine structure and mirror-shape-induced structure is observed. A study of these modes can be used for alignment and characterization of the microcavity [79]. Therefore, it is important to thoroughly understand the physical properties of the cavity modes.

In this chapter, we study optical microcavities using broadband, intracavity emitters. We measure spectra of the fluorescence from these emitters, while slowly tuning the cavity length, resulting in a joined length-wavelength fluorescence spectrum $P(\lambda, L)$. The key message of this chapter is that the analysis of the joined $P(\lambda, L)$ spectrum provides a wealth of information on the cavity and its mirrors. First, we distinguish between the different penetration depths [53] of the mirrors in the cavity. Second, we analyze the spectra of the transverse modes and find from the mode spacings that a shape imperfection of the mirror dominates the mode structure. Last, we zoom in on cavity lengths where the $N = 0$ mode is almost frequency degenerate with the $N = 6$ mode group. We observe an avoided crossing around the wavelength and cavity length where these modes should overlap and quantify it with coupled-mode theory [115, 116].

6.2. SETUP

Figure 6.1 shows a schematic of the experimental setup. The optical cavity, shown in the center, consists of two highly reflective distributed Bragg reflectors (DBR); one flat and the other curved. We use an asymmetric set of mirrors, where the flat mirror has a higher transmission ($T = 1.8(1) \times 10^{-3}$ at $\lambda = 633$ nm, central wavelength $\lambda_c = 640$ nm) than the curve mirror ($T = 0.3(2) \times 10^{-3}$ at $\lambda = 633$ nm, $\lambda_c = 610$ nm), such that most of the fluorescent light leaves the microcavity through the flat mirror. The two mirrors are coated with alternating layers of SiO_2 ($n = 1.46$) and Ta_2O_5 ($n = 2.09$). The curved mirror is a H-DBR, meaning that it ends with a high reflective index layer of Ta_2O_5 to optimize its reflectivity for a given number of layers. The flat mirror, produced by LaserOptik, is an L-DBR ending with a lower refractive index layer of SiO_2, to create a field node close to its surface. The curved mirror, produced by Oxford HighQ [59], has a small radius of curvature $R = 17.7(3)$ μm. We use a hexapod system to align the mirrors in parallel and tune the cavity lengths $L = 3$-10 μm with piezo stacks.

We use nanodiamonds as broadband intracavity emitters. The nanodiamonds (Adamas Nanotechnologies FND, 40 nm, 1-4 NV^- per nanodiamond) contain NV^- and NV^0 centers whose combined room-temperature emission spectrum (590-700 nm) overlaps with the stopband of our cavity (590-680 nm). The nanodiamonds are drop-casted onto the flat mirror. Their concentration is not uniform and we scan the flat mirror to find an optimum where there are enough emitters to make the signal-to-noise ratio large enough, but not too many to introduce too much scattering loss and reduce the finesse too far below $F \approx 1000$.

In the first experiment, we inject the cavity with a HeNe laser ($\lambda = 633$ nm) to probe the finesse and "length spectrum" of the cavity. We couple the laser light into the cavity with a $f_1 = 5$ mm (40X, NA=0.6) lens, and out of the cavity with a $f_2 = 8$ mm (NA=0.5) aspheric lens. We rapidly scan the cavity length (scan velocity $\approx 10\mu$m/s) and record the transmission spectrum on a solid-state photomultiplier tube (PMT). From this scan, we determine a finesse of $F \approx 1000$ for the fundamental modes. Furthermore, we use it to compare the mode structure of a length scan with that of a spectral scan (see below).

In the second set of experiments, which form the bulk of this chapter, we measure the fluorescence spectrum from the cavity. We use a frequency-doubled Nd:YAG-laser (λ =532 nm) to excite intracavity emitters. We measure their fluorescence spectrum with two different spectrometers. The first (fiber-coupled) spectrometer (Ocean Optics QE65000) can

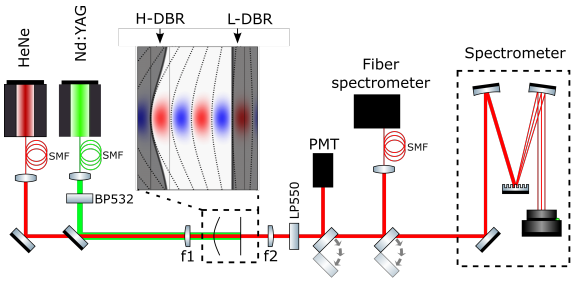

Figure 6.1: Schematic image of the experimental setup. The microcavity (center + zoom-in) is injected with either a HeNe laser (λ = 633 nm) or a Nd:YAG laser (λ = 532 nm). The fluorescence spectra under green off-resonant excitation are observed either with a fiber spectrometer (not shown) or a free space spectrometer. A 10 nm bandpass filter around 532 nm (BP532) is used to filter out fluorescence that may originate from the fiber. A 550 nm longpass filter (LP550) is used to block the green laser light transmitted through the cavity.

image the full fluorescence spectrum with a resolution of $\lambda_{\text{res}} = 0.4$ nm. The second (free-space) spectrometer has a smaller spectral range (619-647 nm) but a better spectral resolution of $\lambda_{\text{res}} = 0.05$ nm, which is comparable to typical linewidths in the cavity fluorescence spectrum. The photoresponse of this spectrometer is about 1 bitcounts per outcoming cavity photon (the CCD has approx. 8 bitcounts/photon and approx. $\frac{1}{8}$ transmission from cavity to CCD). The cavity length is now scanned very slowly (scan velocity ≈ 0.3 nm/s) such that the cavity resonances appear to be quasi-static. The 1 Hz acquisition rate of the spectrometer is just fast enough to minimize the influence of drift on the measurements.

6.3. JOINED LENGTH-WAVELENGTH SCAN

Figure 6.2 shows a typical fluorescence spectrum $P(\lambda, L)$ of the emitters in the cavity. This data is measured by slowly increasing the cavity length L, while constantly recording the emission spectrum on a spectrometer. Each vertical linecut corresponds to a single measurement at fixed L. The linecut for $L \approx 3.6$ μm is shown as the black curve on the right. The righthand figure also shows a red curve which is the emission spectrum of the NV centers averaged over a large range of cavity lengths ($L = 3.0 - 5.2$ μm). This shows that the spectrum is relatively uniform over the investigated wavelength range. The cavity length is estimated by taking a horizontal linecut, as plotted in the top of Fig. 6.2, and fitting the transverse mode splittings to an increasing Gouy phase (see also ref. [53]). The shortest cavity length is $L \approx 2.9$ μm, indicated by the yellow line, where the substrates of the mirrors almost touch.

The optical modes in Fig. 6.2 can be labeled by a longitudinal mode number q and a transverse mode number N. The longitudinal mode number q and cavity length L are estimated based on the mode crossing of the fundamental $N = 0$ mode with the $N = 6$ mode, where $L + 2L_D = R\sin(\pi/6)^2 = R/4$. The physical cavity length L is then determined by filling in the values L_D and R from the fits in Fig. 6.3 below. The number of half-wavelengths that fit in this cavity length results in a longitudinal mode number $q = 2L/\lambda = 13.1(3)$ for the fundamental mode at this crossing at $\lambda = 637$ nm. The large uncertainty in q is due to the difficulty to determine the radius of curvature and modal penetration depth for all

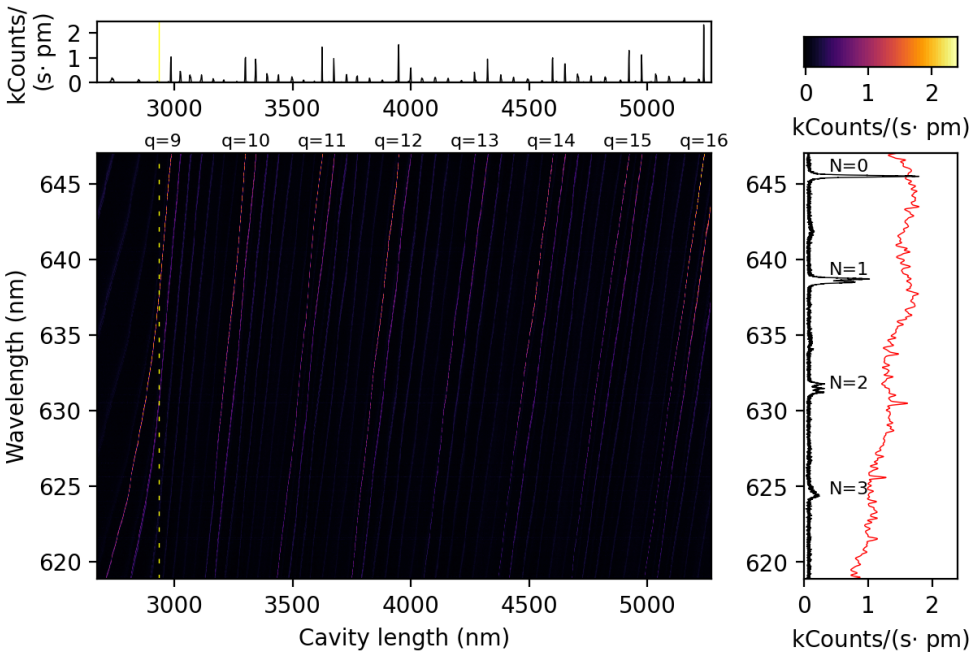

Figure 6.2: Emission spectrum $P(\lambda, L)$ of NV centers in the optical cavity: (middle) false-color plot of the fluorescence spectra as a function of the cavity length, (right, black curve) typical spectrum for $q = 11$ at $L \approx 3.6$ μm, (right, red curve) emission spectrum averaged over $L = 3.0 - 5.2$ μm, (top) horizontal linecut for $\lambda = 646$ nm.

longitudinal mode numbers simultaneously. For a combination of a H-DBR and L-DBR, we expect q to be a half-integer [53]. However, due to the asymmetry of the mirror stopbands and slightly thinner final layer of the L-DBR, the reflection phase of the L-DBR is non-zero, which results in an unconventional value of q. For labeling purposes, we round q to integer values. The exact value of q has no influence on the measurements shown below but will be discussed in more detail in the Appendix.

6.4. PENETRATION DEPTHS

The frequency- and angle-dependent reflection of any DBR can be described by three penetration depths: L_φ, L_τ and L_D [53]. The phase penetration depth L_φ is the shift of the (anti-)node when the frequency ν is detuned from the DBR's central frequency ν_c. The frequency penetration depth L_τ is the extra length required to correct for the time delay of a reflected laser pulse. The modal penetration depth L_D describes the shift of the focus of a converging beam inside the mirror. The penetration depths are different for H-DBRs and L-DBRs [53, 54];

$$L_\tau = \frac{1}{n_H - n_L}\frac{\lambda_c}{4} \text{ (H-DBR)} \qquad L_\tau = \frac{n_H n_L}{n_H - n_L}\frac{\lambda_c}{4} \text{ (L-DBR)} \tag{6.1}$$

where n_H and n_L are the high and low refractive indices of the DBR pairs. The modal penetration is related to the frequency penetration depth [53, 55], as;

$$L_D = \frac{L_\tau}{2}\left(\frac{1}{n_H^2} + \frac{1}{n_L^2}\right). \tag{6.2}$$

Both equations assume that the DBR is illuminated from air ($n = 1$). The phase penetration depths is frequency dependent, $L_\varphi = \frac{\nu - \nu_c}{\nu} L_\tau$, where ν_c is the central frequency of the stopband. The penetration depths of the two different mirrors used here are referred to as $L_{\tau,1}, L_{\tau,2}, L_{D,1}, L_{D,2}$.

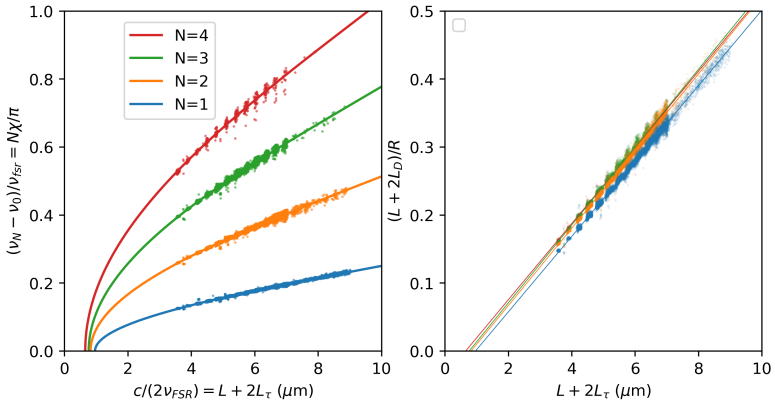

Figure 6.3: The Gouy phase of the first 4 transverse mode groups as a function of the inverse of the free spectral range. The Gouy phase χ is determined from the transverse mode splitting. The free spectral range ν_{fsr} is determined from the distance between two subsequent fundamental modes. The right figure shows the data from the left figure after conversion of the vertical scale from $N\chi/\pi$ to $\sin^2(\chi) = (L+2L_D)/R$.

The frequency spacing between consecutive fundamental modes and the spacing between transverse modes depend on different penetration depths. This can be seen from the cavity resonance condition [53],

$$\frac{2L}{c}\nu + \frac{2(L_{\tau,1} + L_{\tau,2})}{c}(\nu - \nu_c) = q + (N+1)\frac{\chi}{\pi}, \tag{6.3}$$

where L is the physical (on-axis) distance between the two mirrors, c is the speed of light, and χ is the Gouy phase (see below). The frequency difference between two consecutive fundamental modes at fixed L, the so-called free spectral range, depends only on the frequency penetration depth,

$$\nu_{q+1,0} - \nu_{q,0} = \nu_{\mathrm{fsr}} = \frac{c}{2(L + L_{\tau,1} + L_{\tau,2})} \quad \Longrightarrow \quad L + L_{\tau,1} + L_{\tau,2} = \frac{c}{2(\nu_{q+1,0} - \nu_{q,0})} \tag{6.4}$$

The transverse mode spacings and the associated Gouy phase χ, on the other hand, depend only on the modal penetration depth [53] via

$$\pi\frac{\nu_{q,N} - \nu_{q,0}}{N\nu_{\mathrm{fsr}}} = \chi = \arcsin\sqrt{\frac{L + L_{D,1} + L_{D,2}}{R}} \quad \Longrightarrow \quad \frac{L + L_{D,1} + L_{D,2}}{R} = \sin^2\left(\frac{\pi}{N}\frac{\nu_{q,N} - \nu_{q,0}}{\nu_{q+1,0} - \nu_{q,0}}\right). \tag{6.5}$$

6

From the difference between these quantities, we find the difference between the penetration depths of the mirror pair $L_{\tau,1}+L_{\tau,2}-L_{D,1}-L_{D,2}$, without having to rely on an absolute longitudinal mode number q.

Figure 6.3 shows the measurements of the two different penetration depths. These were measured using the fiber spectrometer with the larger spectral range. We only use cavity modes between $\lambda = 610-670$ nm such that a non-linearity in the reflection phase of the DBR is relatively small [61]. The data in the figure are corrected for this 3$^{\text{rd}}$-order non-linearity (corrections are ≤20%, see Appendix 6.A. The horizontal axis indicates the cavity length, as determined by the inverse of the free spectral range. The vertical axis shows the transverse mode splittings, normalized to the free-spectral range. The increasing spread in points for higher N is mainly due to weaker peaks, making them more difficult to distinguish from the noise.

The difference in penetration depths $L_\tau - L_D$ is visible as the crossing with the x-axis in Fig. 6.3. This can be seen best in Fig. 6.3b. A linear fit of Fig. 6.3b gives penetration depths for transverse modes $N = 1-4$ of $(L_{\tau,1}+L_{\tau,2}-L_{D,1}-L_{D,2})/2 = 0.481(2)$, 0.410(2), 0.381(3), 0.33(1) μm. The radii of curvature are $R = 18.02(1)$, 17.60(1), 17.45(2), 17.84(9) μm. From theory [53] we expect that the H-DBR (curved mirror) has a penetration depth $L_\tau = 0.25$ μm, and the L-DBR a penetration depth $L_\tau = 0.77$ μm. This means that the theoretical difference in penetration depths $(L_{\tau,1}+L_{\tau,2}-L_{D,1}-L_{D,2})/2 = 0.33$ μm. The measured values of Ł$_\tau - L_D$ agree reasonably well with theoretical predictions. Still, the measured values are somewhat larger than predicted. This might be due to the asymmetric mirror set with different central wavelengths. The data also suggests N-dependent variations in curvature and penetration depths, possibly due to mirror shape effects [94], where each transverse mode scans a different part of the curve mirror.

6.5. TRANSVERSE MODE GROUP STRUCTURE

Figure 6.4 shows the zoomed-in spectra of the transverse mode groups $N = 1$ to $N = 4$. The $N = 1$ and $N = 2$ groups were measured at $q = 11$, where the modes are the least coupled to any other transverse mode groups. The $N = 3$ and $N = 4$ transverse groups were measured at $q = 8$ where the two mirrors almost touch, such that vibrations are smaller and the peaks become better resolvable. Each transverse mode group N is predicted to consist of $N+1$ separate peaks. The observed number of peaks in the $N = 3$ and $N = 4$ spectra is N instead of the expected $N+1$, presumably because one peak overlaps with the others.

Table 6.1: Mode structure, relative to the free spectral range, determined from (i) emission spectra at fixed cavity length, (ii) length scans at fixed wavelength (λ = 633 nm), and (iii) theoretical values for a perfectly spherical mirror. The $N = 1$ structure contains only two peaks, whereas the $N = 2$ structure contains three peaks. The two distances for $N = 2$ are (a) and (b) as indicated in Fig. 6.4.

	Spectral: $\Delta\lambda/\lambda_{\text{fsr}}$	Length scan: $\Delta L/(\lambda/2)$	Theory: $\Delta\varphi_{th}/(2\pi)$
N=1	$5.35(2)\times10^{-3}$	$5.1(6)\times10^{-3}$	1.78×10^{-3}
N=2 (a)	$5.63(5)\times10^{-3}$	$6.6(6)\times10^{-3}$	2.78×10^{-3}
N=2 (b)	$12.05(5)\times10^{-3}$	$13(1)\times10^{-3}$	3.56×10^{-3}

The measured transverse group structure is quantified by determining the distance

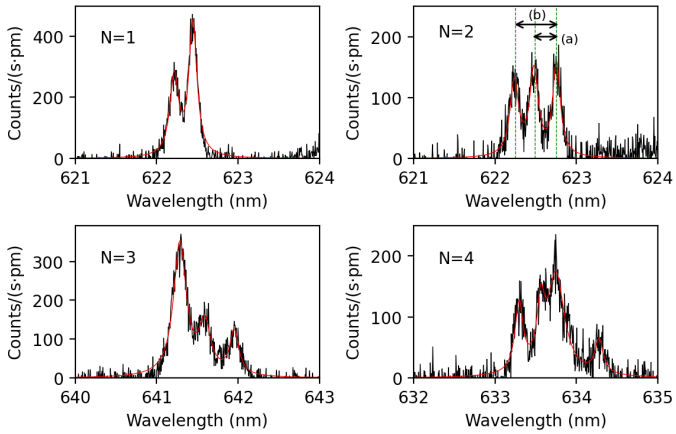

Figure 6.4: Mode structure for transverse mode groups $N = 1-4$. Each transverse mode group is fitted with 2, 3, 3 and 4 Lorentzians for the $N = 1, 2, 3$ and 4, respectively. The $N = 2$ plot show peak distances that correspond to the (a) and (b) labels in Table 6.1.

between the peaks. In the case of a perfectly spherical mirror, the mode structure is determined by a fine structure, $\Delta\lambda/\lambda_{\text{fsr}} = (\ell \cdot s + 3\ell^2/8)/(2\pi kR)$, where ℓ and s are the angular momentum and spin polarization of the mode [88, 110]. For the $N = 1$ and $N = 2$ mode groups, we observe the expected number of peaks, so we can make a comparison between theory and measurement. Table 6.1 shows this comparison, where we also added the splitting from the mode structure measured with a length scan using a HeNe laser.

The advantage of a spectral measurement over a length scan is that it hardly depends on the incoupling of light [88]. Furthermore, it is not influenced by fluctuations in the piezo-velocity, such that the uncertainties are smaller. The mode structure is similar for the spectral and cavity length scan. The theoretically predicted values for the nonparaxial fine-structure, are a factor 2-3 smaller than the measured values, from which we conclude that technical effects dominate over the intrinsic nonparaxial effects. This is most likely due to astigmatism in the curved mirror, which shifts the fundamental fine structure towards more equidistant peaks, observed as for $N = 2$ [88].

6.6. MODE COUPLING

Figure 6.5 shows a false color plot of $P(\lambda, L)$ in the region where the $(q = 13, N = 0)$ and $(q = 12, N = 6)$ modes cross. This is a zoom-in from figure 6.2 around the $q = 13$ longitudinal mode, but the horizontal and vertical axes are interchanged and rescaled. The vertical axis now shows the wavelength $\lambda_{13,0}$ at which an uncoupled $(q = 13, N = 0)$ mode would be resonant. The increasing value of $\lambda_{13,0}$ corresponds to an increasing cavity length in the measurements, which can also be described by an increasing Gouy phase, as shown on the y-axis on the right. The horizontal axis shows the spectrum in terms of wavelength detuning $\lambda - \lambda_{13,0}$. Comparable figures in refs. [31, 49] present data as a function of longitudinal mode number q, i.e. a $P(q, L)$ map is shown instead of a $P(\lambda, L)$ map. The advantage of a $P(\lambda, L)$ map is that λ is a continuous variable and not an integer like q. This is especially

important for small cavities, where the Gouy phase χ changes rapidly with cavity length, and the steps due to discrete changes in q are too large to accurately measure coupling in the length spectra [94].

The accurate determination of $\lambda_{13,0}$ required some refinements of the data. First, we shifted all measured spectra such that the intensity-weighted wavelength around the $N = 0$ and $N = 6$ modes was set to zero. From the resulting image, a straight line could be drawn for the $N = 0$ mode between the highest and lowest wavelengths where the $N = 0$ and $N = 6$ modes are not coupled (see top and bottom of Fig. 6.5). This straight line yields the values $\lambda_{13,0}$ in Fig. 6.5. A Gaussian filter was used to make the $N = 6$ modes (visible as slanted lines) better visible. Without these corrections, the coupling is still visible but less clean.

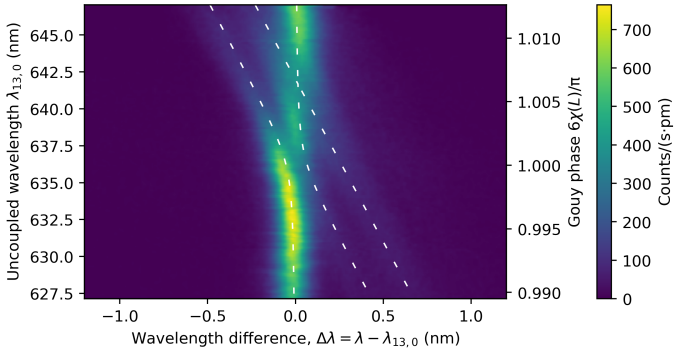

Figure 6.5: False color plot of the fluorescence in the $N = 0$ and $N = 6$ modes around their frequency degeneracy. The vertical axis indicates the cavity-length-dependent wavelength $\lambda_{13,0}$ at which the uncoupled $N = 0$ ($q = 13$) mode is resonant. The horizontal axis indicates the spectral distance $\lambda - \lambda_{13,0}$ from this uncoupled $N = 0$ mode. The white curves follow a theoretical model of coupled modes (see text for details).

We can quantify this avoided crossing using a coupled-mode model with a coupling matrix [94]

$$\begin{pmatrix} 0 & -M \\ -M & \Delta\varphi \end{pmatrix}, \tag{6.6}$$

where $\Delta\varphi = 6\chi - \pi$ is the one-way phase difference between the $N = 6$ and $N = 0$ modes, and M is the coupling parameter. Using a "fit-by-eye" we find $M = 0.014(3)$. This value is similar to the coupling parameter $M = 0.016(2)$ found in a similar cavity [94]. This shows the equivalence between measurements in the frequency-domain and the far-field.

6.7. CONCLUSIONS

We have demonstrated the use of broadband intracavity emitters for the characterization of microcavities. The broadband spectra $P(\lambda, L)$ enable accurate determination of the difference between the two penetration depths $L_\tau - L_D$ without relying on the exact cavity length L or longitudinal mode number q. Furthermore, mode-coupling can be measured without having to switch between discrete values of q. This is crucial in very small cavities, where the Gouy phase changes rapidly with cavity length. The advantage of using

these broadband emitters over a frequency-tunable laser is that they emit directly inside the cavity, which removes potential problems of frequency-dependent incoupling.

The description of mode formation in a microcavity becomes intriguing when microcavities become smaller. For small radii of curvature, the mode spectra require nonparaxial corrections and mode-coupling can be strong for small mirror shape imperfections. Furthermore, the penetration depth can become significant, especially when L-DBRs are used. This is most prominently visible in the difference between two penetration depths $L_\tau - L_D$. When this aspect is overlooked, it can easily result in a wrong estimation of the longitudinal mode number q. The effects of the DBR penetration on the Gouy phase χ are generally smaller, since $L_D \ll L_\tau$, but are still required for a complete description. The full $P(\lambda, L)$ map of the microcavity reveals all these aspects in a single picture.

6.8. ACKNOWLEDGMENTS

We thank A. Trichet from Oxford HighQ for providing the curved mirrors.

6.A. THIRD-ORDER FREQUENCY DISPERSION OF DBRS

This Appendix describes the influence of the third-order frequency dispersion of DBRs on the measurements. For most cases, the reflection phase of the DBR is linearly approximated, $\varphi = \frac{2L_\tau}{c}(\nu - \nu_c)$, with the central frequency ν_c and frequency penetration depth L_τ. If the frequency is near the edge of the DBR stopband, this relation becomes non-linear [61, 62]. This has consequences for the accurate determination of the penetration depths.

The complex reflection amplitude of a DBR can be derived from coupled mode theory [51, 52]. Its frequency dependence can be derived from an expansion of the phase in the reflection amplitude $\Gamma_0 = |\Gamma_0| e^{i\varphi}$ [53], where $|\Gamma_0| = 1$. The result

$$\varphi = \arcsin[\tau_0(\omega - \omega_c)] \approx \tau_0(\omega - \omega_c) + \frac{\tau_0^3(\omega - \omega_c)^3}{6} + \dots , \tag{6.7}$$

with $\tau_0\omega_c = \pi n_H/(n_H - n_L)$, is only valid when the material outside of the DBR has refractive index $n_{in} = n_H$ or $n_{in} = n_L$. For the general case, we need to consider one more reflection from its first layer, such that the new reflection amplitude is

$$\Gamma = -\frac{r \mp \Gamma_0 e^{i2(\omega-\omega_c)\Delta\tau}}{1 \pm r\Gamma_0 e^{i2(\omega-\omega_c)\Delta\tau}}. \tag{6.8}$$

where the $+(-)$-sign is used for an initial layer with low(high) refractive index and $\Delta\tau = \pi/(2\omega_c)$ is the transit time through the first layer. The reflection from the first interface is $r = \frac{n_{in}-n_{L/H}}{n_{in}+n_{L/H}}$. The approximate reflection phase of the mirror including this top layer is

$$\Gamma = |\Gamma| e^{i(\tau_{L/H}(\omega-\omega_c) + \mu_{L/H}(\omega-\omega_c)^3/\omega_c^3)}, \tag{6.9}$$

where $\tau_{L/H}$ and $\mu_{L/H}$ are constants which are determined from the refractive indices of the DBR. The frequency penetration depth is related through $L_{L/H} = \frac{\tau_{L/H}}{2n_{in}}c$. If we assume that $|\Gamma_0| = |\Gamma| = 1$ and compare the first and third derivatives of equations (6.8) and (6.9) as was done in [54] we find for the H-DBR,

$$\omega_c\tau_H = \pi\frac{n_{in}}{n_H}\frac{n_H}{n_H - n_L} \qquad \mu_H = \pi\frac{n_{in}}{6n_H}\left(\frac{n_H}{n_H - n_L}\right)^3 \tag{6.10}$$

and for the L-DBR

$$\omega_c \tau_L = \pi \frac{n_L}{n_{in}} \frac{n_H}{n_H - n_L} \qquad \mu_L = \pi \frac{n_L}{6 n_{in}} \left(\frac{n_H}{n_H - n_L} \right)^3 . \tag{6.11}$$

For our mirrors, with $n_L = 1.46$ and $n_H = 2.09$, we expect $\mu_H = 9.1$ and $\mu_L = 27.9$.

The resonance condition of the cavity, including the third-order non-linearity of the DBR is

$$\nu \frac{2L}{c} = q + (N+1)\chi/\pi - \frac{2(L_{\tau,1} + L_{\tau,2})}{c}(\nu - \nu_c) - \mu \frac{(\nu - \nu_c)^3}{\nu_c^3}, \tag{6.12}$$

which is an extended version of Eq. (6.3) in the main text. $\mu = \mu_1 + \mu_2$ is the combined non-linearity constant of both mirrors. The free spectral range $\nu_{\text{fsr}} = \nu_{q+1,0} - \nu_{q,0}$ in this case is given by;

$$\nu_{\text{fsr}} \frac{2(L + L_{\tau,1} + L_{\tau,2})}{c} = 1 - \mu \frac{(\nu_{q+1,0} - \nu_c)^3 - (\nu_{q,0} - \nu_c)^3}{\nu_c^3} \approx 1 - 3\mu \frac{\nu_{\text{fsr}}}{\nu_c} \left(\frac{\nu - \nu_c}{\nu_c} \right)^2, \tag{6.13}$$

which is an extended version of Eq. (6.4) in the main text. We can express this in terms of an effective cavity length L_{eff} normalized by the averaged frequency $\overline{\nu} = (\nu_{q+1,0} + \nu_{q,0})/2$

$$\frac{\overline{\nu}}{\nu_{\text{fsr}}} = \frac{L_{\text{eff}}}{\lambda/2} \approx q + \frac{1}{2} + \frac{2(L_{\tau,1} + L_{\tau,2})}{c} \nu_c + 3\mu \left(\frac{\overline{\nu} - \nu_c}{\nu_c} \right)^2 \frac{\overline{\nu}}{\nu_c}, \tag{6.14}$$

where $q + 1/2$ is the average q of two subsequent fundamental modes, $\frac{2(L_{\tau,1}+L_{\tau,2})}{c}\nu_c$ originates from the linear frequency dispersion, and the final term is a third-order correction to the frequency penetration depth.

Figure 6.6a shows the observed effective cavity lengths, expressed in units $\lambda/2$. Each curve is one longitudinal mode number higher, as expected. Furthermore, the parabolic trend from equation (6.14) is visible. This parabola is better visible in Fig. 6.6b, where all curves are shifted by $q + 1/2$ and now lie on top of each other. A simultaneous fit of all data with Eq. (6.14), yields a non-linearity factor $\mu = 48.3(6)$ and a central frequency $\lambda_c = 635(1)$ nm ($\nu_c = 472.5(8)$ THz). The measured value for μ agrees reasonably well with the theoretically predicted value of $\mu = \mu_H + \mu_L = 37.0$. But the central wavelength is surprisingly close to the central wavelength of the H-DBR, $\lambda_c = 640$ nm ($\nu_c = 469$ THz). From theory, one would expect the central wavelength to be closer to the L-DBR, $\lambda_c = 610$ nm ($\nu_c = 492$ THz), since its value for μ_L is larger than μ_H. This discrepancy from theory might be due to the large spread in data points near 610 nm, where the NV centers are less bright.

The offset of the parabola in Fig. 6.6b contains information about L_τ. The figure shows the effective cavity length $\overline{\nu}/\nu_{\text{fsr}}$, divided by $\lambda/2$ and shifted by $q + 1/2$. In contrast to the main text, the exact value of q is now important. The q that is subtracted is the same integer value that is used for labeling in the main text and in Fig. 6.6, but this is not entirely correct. For the combination of an ideal L-DBR and H-DBR, we expect q to be half-integer [53], but for our L-DBR, with a top layer of $0.8 \times \lambda_c/(4n_L)$ instead of $\lambda_c/(4n_L)$, we expect a slightly different q. The best experimental estimate of the longitudinal mode number is $q = 13.1(3)$ given in the main text, which is thus 0.1(3) more than the integer labels used to convert Fig. 6.6a to Fig. 6.6b. Therefore, if we want to interpret the vertical axes of Fig. 6.6b correctly, we should subtract an additional 0.1(3), which we then

use to roughly estimate the penetration depth from the offset value in Fig. 6.6b to be $\frac{2(L_{\tau,1}+L_{\tau,2})}{c}\nu_c \approx 2.5(3)$ or $L_{\tau,1}+L_{\tau,2} \approx 0.8(1)$ μm. This is somewhat smaller than the theoretical prediction $\frac{2(L_{\tau,1,th}+L_{\tau,2,th})}{c}\nu_c = 3.20$ or $L_{\tau,1,th}+L_{\tau,2,th} = 1.02$ μm ($L_{\tau,1,th} = 0.77$ and $L_{\tau,2,th} = 0.25$). The measurements in the main text do not rely on q and are thus a more reliable measurement of the penetration depth.

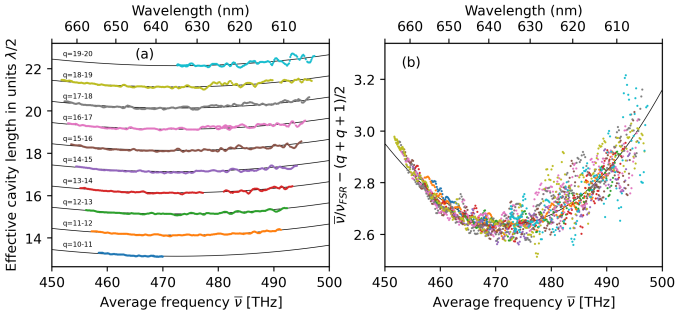

Figure 6.6: Effective cavity length, L_{eff}, calculated from the free spectral range between the $N = 0$ modes with q and $q+1$, where $q = 10-19$ are indicated with different colors. The points at a higher average frequency are more noisy because the intracavity NV centers are less bright. (a) Original data, (b) all data shifted by $q+1/2$, where q is the lowest number in the labels $q = 10-11$, $q = 11-12$ etc. in (a).